Advanced fluorescence microscopy reveals disruption of dynamic CXCR4 dimerization by subpocket-specific inverse agonists

Ali Işbilir[a,b], Jan Möller[a,b], Marta Arimont[c], Vladimir Bobkov[c,d], Cristina Perpiñá-Viciano[b,e], Carsten Hoffmann[b,e], Asuka Inoue[f], Raimond Heukers[c,g], Chris de Graaf[c,h], Martine J. Smit[c], Paolo Annibale[a,b,1], and Martin J. Lohse[a,b,i,1]

[a]Receptor Signaling Group, Max Delbrück Center for Molecular Medicine, 13125 Berlin, Germany; [b]Institute of Pharmacology and Toxicology, University of Würzburg, 97078 Würzburg, Germany; [c]Amsterdam Institute of Molecular and Life Sciences (AIMMS), Vrije Universiteit Amsterdam, 1081 HZ Amsterdam, The Netherlands; [d]argenx BVBA, Zwijnaarde 9052, Belgium; [e]Institute of Molecular Cell Biology, University Hospital Jena, University of Jena, 07745 Jena, Germany; [f]Graduate School of Pharmaceutical Sciences, Tohoku University, 980-8578 Sendai, Japan; [g]QVQ Holding B.V., 3584 CL Utrecht, The Netherlands; [h]Sosei Heptares, CB21 6DG Cambridge, United Kingdom; and [i]ISAR Bioscience Institute, 82152 Munich, Germany

Edited by Robert J. Lefkowitz, Howard Hughes Medical Institute, Durham, NC, and approved September 28, 2020 (received for review June 26, 2020)

Although class A G protein–coupled receptors (GPCRs) can function as monomers, many of them form dimers and oligomers, but the mechanisms and functional relevance of such oligomerization is ill understood. Here, we investigate this problem for the CXC chemokine receptor 4 (CXCR4), a GPCR that regulates immune and hematopoietic cell trafficking, and a major drug target in cancer therapy. We combine single-molecule microscopy and fluorescence fluctuation spectroscopy to investigate CXCR4 membrane organization in living cells at densities ranging from a few molecules to hundreds of molecules per square micrometer of the plasma membrane. We observe that CXCR4 forms dynamic, transient homodimers, and that the monomer–dimer equilibrium is governed by receptor density. CXCR4 inverse agonists that bind to the receptor minor pocket inhibit CXCR4 constitutive activity and abolish receptor dimerization. A mutation in the minor binding pocket reduced the dimer-disrupting ability of these ligands. In addition, mutating critical residues in the sixth transmembrane helix of CXCR4 markedly diminished both basal activity and dimerization, supporting the notion that CXCR4 basal activity is required for dimer formation. Together, these results link CXCR4 dimerization to its density and to its activity. They further suggest that inverse agonists binding to the minor pocket suppress both dimerization and constitutive activity and may represent a specific strategy to target CXCR4.

GPCR | chemokine receptor | dimerization | basal activity | microscopy

G protein–coupled receptors (GPCRs) constitute the largest class of cell surface receptors and are the main targets of clinically approved drugs (1). While GPCRs have classically been thought to exist and function as simple monomers, substantial data show that many of them may form dimers and higher-order oligomers, which might be relevant for their function (2). In particular, it is now well-appreciated that class C GPCRs form obligatory dimers (3) and that intermolecular rearrangements of such dimers play a key role for receptor activation (4, 5). Even though members of the much larger family of class A GPCRs have been shown to transduce signals as monomeric entities (6), emerging evidence demonstrates that they can form oligomers both in vitro and in vivo (7, 8). Several recent studies using advanced fluorescence microscopy methods suggested a dynamic nature of dimerization for a number of class A GPCRs (9–12). Thus, the stability, dynamics and functional relevance of individual class A GPCR dimers remains debatable.

The CXC chemokine receptor 4 (CXCR4) is a prime example of a class A GPCR where the quaternary organization may be functionally and pharmacologically important. While CXCR4 regulates physiological processes mainly associated with cell migration and development, dysregulation of CXCR4 expression and function plays an important role in cancer progression, as well as viral and immune diseases (13). Following the discovery of two ligand binding pockets (major and minor) of CXCR4, several drugs targeting this receptor have been studied (14). With one marketed and others in clinical trials, CXCR4 drugs receive substantial interest for numerous diseases (15).

Multiple studies using fluorescence-based methods described CXCR4 oligomerization ranging from expression-dependent complex formation to stable and ligand-independent CXCR4 homodimers and homooligomers (16, 17). Agonist binding was proposed to induce conformational changes between the CXCR4 protomers (18) and even to induce higher-order complexes (19).These agonist-induced CXCR4 nanoclusters were suggested to define cellular functions of CXCR4, and mutations that alter the cluster organization also inhibit receptor signaling in vivo (19). CXCR4 dimerization was also described in malignant cells (20). Moreover, CXCR4 crystal structures with three different ligands displayed dimeric units with similar interfaces (21, 22). Although a 1:1 stoichiometry between CXCR4 and its

Significance

Class A G protein–coupled receptors (GPCRs) can form dimers and oligomers via poorly understood mechanisms. We show here that the chemokine receptor CXCR4, which is a major pharmacological target, has an oligomerization behavior modulated by its active conformation. Combining advanced, single-molecule, and single-cell optical tools with functional assays and computational approaches, we unveil three key features of CXCR4 quaternary organization: CXCR4 dimerization 1) is dynamic, 2) increases with receptor expression level, and 3) can be disrupted by stabilizing an inactive receptor conformation. Ligand binding motifs reveal a ligand binding subpocket essential to modulate both CXCR4 basal activity and dimerization. This is relevant to develop new strategies to design CXCR4-targeting drugs.

Author contributions: A. Işbilir, P.A., and M.J.L. designed research; A. Işbilir, J.M., and M.A. performed research; V.B., A. Inoue, R.H., and M.J.S. contributed new reagents/analytic tools; A. Işbilir, J.M., and P.A. analyzed data; and A. Işbilir, C.P.-V., C.H., C.d.G., P.A., and M.J.L. wrote the paper.

The authors declare no competing interest.

This article is a PNAS Direct Submission.

[1]To whom correspondence may be addressed. Email: Paolo.Annibale@mdc-berlin.de or m.lohse@mdc-berlin.de.

This article contains supporting information online at https://www.pnas.org/lookup/suppl/doi:10.1073/pnas.2013319117/-/DCSupplemental.

First published November 4, 2020.

main endogenous chemokine ligand, CXCL12, was shown to be sufficient for signal transduction (23), others reported homomeric CXCR4 complexes as functionally distinct units (24). Altogether, there is no clear picture of how and to what extent CXCR4 oligomerizes and how oligomerization is modulated. However, such an understanding would be needed as a basis to define druggable sites as well as ligands for this clinically important receptor.

Here, we combine advanced microscopy methods—single-molecule microscopy and fluorescence fluctuation spectroscopy—to explore the quaternary organization of CXCR4 in living cells, at different expression levels and both under basal conditions and in the presence of diverse, chemically distinct CXCR4 ligands. We observe a transient formation of CXCR4 homodimers, which is dynamic, depends on expression levels, and is specifically disrupted by inverse agonists that bind to the minor subpocket of the receptor. Our data suggest a possible link between receptor dimerization and the basally active state of CXCR4.

Results

CXCR4 Is Largely Monomeric at Low Expression Levels and Forms Transient Homodimers. CXCR4 expression in blood cells ranges from a few thousand to >100,000 receptors per cell [which corresponds to ∼4 to >300 receptors per μm^2 of membrane area, assuming a surface area of a T cell at ∼250 μm^2 (25)] (26, 27). To investigate CXCR4 oligomerization at low expression levels, we used a high spatial resolution method based on total internal reflection fluorescence microscopy (TIRFM), which allowed us to resolve and visualize receptors at single-molecule precision (Fig. 1). For this purpose, we used single images of an N-terminally SNAP-tagged CXCR4 (SNAP-CXCR4), transiently transfected in Chinese hamster ovary (CHO) cells and labeled with SNAP-Surface 549 dye (Fig. 1*A*). For comparison, SNAP-β_1-adrenergic receptor (SNAP-β_1AR) was used as a monomeric control, and SNAP-CD28 as a constitutively dimeric control, as described previously (9, 12). Our previous work reported over 90% labeling efficiency using this strategy (28, 29). From individual TIRF images (Fig. 1*A*), we detected single point spread functions (*SI Appendix*, Fig. S1) and plotted their intensity distributions. Mixed Gaussian fitting on these intensity distributions revealed that, at densities below 0.3 particles per μm^2 [which corresponds to ∼200 receptors per cell, assuming a surface area of a CHO cell at ∼700 μm^2 (30)], SNAP-β_1AR was largely monomeric (94.4% monomeric vs. 5.6% dimeric fraction) (Fig. 1*C*), while SNAP-CD28 displayed a 92.6% dimeric and 3.8% tetrameric population, with a monomer fraction at 3.6% (Fig. 1*D*). For SNAP-CXCR4, we observed mostly monomers (86.7%), an 11.6% dimeric population, and a negligible fraction of higher-order oligomers (Fig. 1*B*). These results suggest that SNAP-CXCR4 exhibits a prevalently monomeric behavior at low concentrations in living CHO cells.

Next, we assessed the spatiotemporal dynamics of CXCR4–CXCR4 interactions by TIRF-based single-particle tracking. TIRF image series recorded with high temporal resolution (10- to 50-ms time intervals) allowed us to track the lateral movements of individual single molecules, and thereby to quantify lifetimes of particle colocalization (Fig. 1*E*) within the short observation window that is possible with single-particle tracking (up to 15 s).

Colocalization events observed in such single-molecule tracks are composed of specific dimerization events and random colocalizations (28). Our previous observations from simulated particles with the diffusion profiles of receptors in the absence of specific interactions yielded a tau (τ) value of 112 ms for the lifetime of random colocalizations (29). To distinguish the kinetics of random colocalizations from real SNAP-CXCR4 homodimerization events, we fitted a biphasic exponential decay function to the histogram of dimer lifetimes (Fig. 1*F*), constraining the τ-value of the fast component (representing random colocalizations) to 112 ms. The resulting slow component exhibited a τ-value of 890 ms, revealing a component of true CXCR4–CXCR4 interactions (Fig. 1*F*). The lifetime of such dimers is, thus, approximately 2 times longer than that seen for the largely monomeric μ-opioid receptors (∼460 ms) under analogous conditions (29).

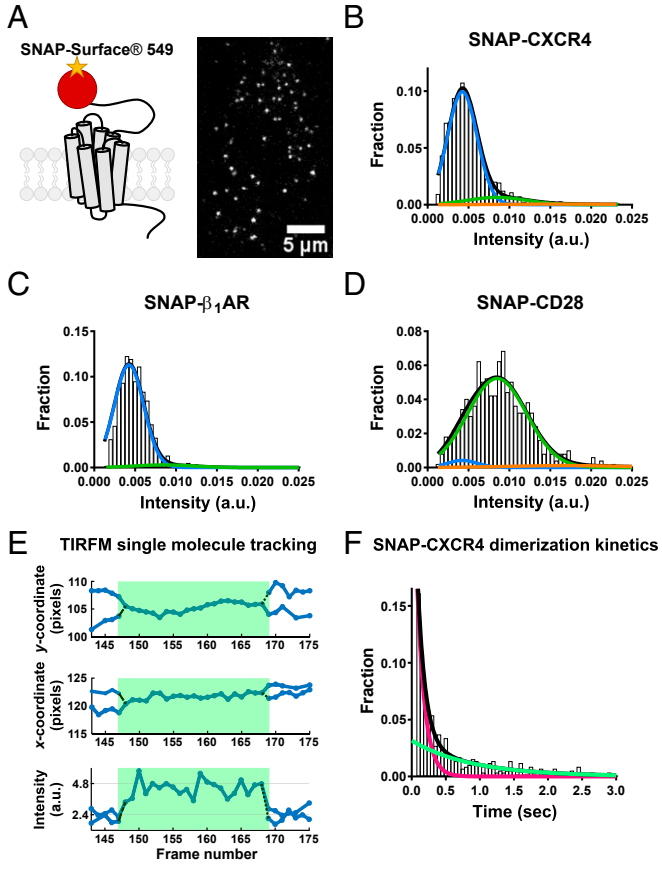

Fig. 1. Single-particle tracking analysis reveals dynamic, transient CXCR4 homodimerization. (*A*) Schematic view of SNAP (red)-CXCR4, labeled with SNAP-Surface 549 (yellow), and a representative single-molecule TIRFM image in an intact CHO-K1 cell. (*B–D*) Intensity distributions of SNAP-Surface 549 particles corresponding to (*B*) SNAP-CXCR4, (*C*) SNAP-β_1AR, and (*D*) SNAP-CD28. A mixed Gaussian fit distinguishes fractions of oligomeric populations. From the global fit (black line), monomeric (blue), dimeric (green), and tetrameric (orange) fractions were derived. Intensity values were collected from 27 different cells for SNAP-CXCR4, 8 cells for SNAP-β_1AR, and 13 cells for SNAP-CD28 in seven independent experiments. (*E*) A representative single receptor track of transient SNAP-CXCR4 homodimerization. Shown are the coordinates of two SNAP-CXCR4 tracks (blue lines) within an image series in X (*Upper*) and Y (*Middle*) dimensions. Intensity doubling (*Lower*) upon particle merging (color change from blue to green) demonstrates receptor interactions. (*F*) Distribution of colocalization times obtained from the length of individual merging–splitting events as in E. A biexponential decay function (black) with a constrained rate constant (magenta), derived from simulated randomly colocalizing particles (magenta), resulted in a slow component (green), representing specific interactions of SNAP-CXCR4, with a lifetime (τ-value) of 890 (730 to 1,088) ms (mean and 95% CI).

Overall, these results indicate that, at low expression levels, SNAP-tagged CXCR4 in living cells are largely monomeric. Such low expression levels allowed us to observe the dynamics of individual receptor–receptor interactions, which revealed that the average lifetime of the few dimers is on the order of 1 s.

Increasing Density Drives CXCR4 toward Homodimers. Having demonstrated that, at low expression levels, CXCR4 are largely

monomeric with only transient dimerization events, we sought to investigate how this might change with increasing receptor densities. Assessing CXCR4 oligomerization at higher levels is of interest both physiologically and pathologically, since several cancer cells express high levels [>50,000 CXCR4 molecules per cell, i.e., >70 receptors per μm^2 of membrane area (31, 32)]. TIRFM-based single-particle analysis is limited to low expression levels, as the spatial separation of individual single molecules is lost at higher particle densities (29). Therefore, to explore CXCR4 oligomerization at higher expression levels, we used a completely different optical approach.

Spatial intensity distribution analysis (SpIDA) (33) is a fluorescence fluctuation spectroscopy method that calculates the density and the quantal brightness of fluorescently labeled molecules from confocal microscopy images. These two values are used to quantify the average oligomeric state of the protein of interest. We used a C-terminally EYFP-tagged β_1AR as a monomeric control, as we had confirmed its monomeric behavior even at overexpression levels (9, 34). In addition, a β_1AR with two adjacent C-terminal EYFP tags (separated by an $(EAAAK)_4$ linker) was employed as a "dimeric" control (34) (Fig. 2*A*). We performed imaging at the basolateral membranes of individual HEK293AD cells expressing the respective fluorescently labeled constructs. For image analysis, we avoided selecting large membrane regions, as well as areas with heterogeneous fluorescent distributions, which are not associated with true receptor oligomers (Fig. 2*A*) (35). SpIDA analysis of controls revealed that the brightness values obtained for β_1AR-2xEYFP were twice those of β_1AR-EYFP (Fig. 2*B*). At different expression levels ranging from 15 to 120 molecules per μm^2 of membrane area, these brightness values remained constant (Fig. 2*C*).

Stepwise photobleaching with SpIDA further confirmed the reliability of our control constructs: If a particular fluorescently labeled protein is truly monomeric, photobleaching will decrease the number of fluorescent particles, without affecting their brightness (33). SpIDA, after photobleaching of β_1AR-EYFP, showed that the brightness did not change even after 10 frames, although the density of fluorescent particles decreased (*SI Appendix*, Fig. S2 *A* and *B*). This confirms again the monomeric character of β_1AR-EYFP. For β_1AR-2xEYFP, we observed a decrease in brightness in parallel with a decrease in their number (*SI Appendix*, Fig. S2 *C* and *D*).

Having established these controls, we then focused on CXCR4. Since HEK293 cells have been reported to express endogenously very low levels of CXCR4 (36), we first assessed the endogenous levels of CXCR4 in our specific HEK293AD cell line, using a fluorophore conjugated antibody that recognizes a specific epitope on CXCR4 (*SI Appendix*, Fig. S3*A*). We observed a fluorescence signal from the antibody in CXCR4-ECFP transfected cells, but not in control cells (*SI Appendix*, Fig. S3*B*). This indicates endogenous CXCR4 expression in our HEK293AD cell is below the detection limit of our SpIDA approach (less than five receptors per square micrometer of membrane area).

SpIDA revealed a density-dependent dimerization profile of CXCR4-EYFP (Fig. 2*C*). We observed brightness values between the monomeric and the dimeric controls within the range of 10 to 30 receptors per μm^2 density [7 to 20,000 receptors per cell, assuming a surface area of a HEK293 cell at 700 μm^2 (37)] (*SI Appendix*, Fig. S2*E*). Analysis within the range of 85 to 150 receptors per μm^2 (60,000 to 105,000 receptors per cell) resulted in an average oligomeric state corresponding to that of the dimeric control (*SI Appendix*, Fig. S2*F*), pointing out a concentration dependence of CXCR4 dimers. To quantify this concentration dependence, we binned CXCR4-EYFP oligomeric state values obtained from SpIDA (Fig. 2*C*). Combining these results with those observed in single-molecule analyses, we calculated that CXCR4 dimerizes with a dissociation constant of about 30 molecules per μm^2 (Fig. 2*D*). This analysis also reveals that CXCR4 is mainly dimeric at oncogenic expression levels (>70 receptors per μm^2 of membrane area, or 50,000 receptors per cell).

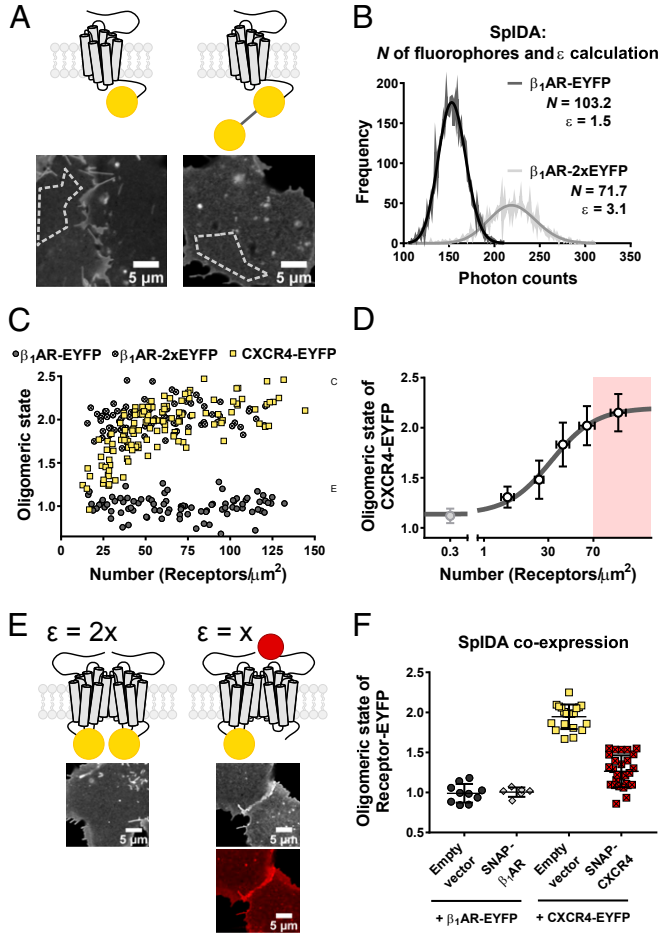

Fig. 2. SpIDA analysis reveals density-dependent formation of metastable CXCR4 dimers. (*A*) Schematics of the monomer (β_1AR-EYFP)/dimer (β_1AR-2xEYFP) controls (EYFP as yellow balls), with their representative basolateral membrane confocal images. Homogeneous membrane areas (gray polygons as ROIs) were analyzed. (*B*) Representative fluorescence intensity distribution (obtained from images as in *A*; dark gray for β_1AR-EYFP and light gray for β_1AR-2xEYFP) with Super-Poissonian fitting to calculate number (*N*) and brightness (ε). (*C*) Measured average oligomeric state per cell as a function of fluorescent particle number. Each data point represents the brightness value obtained from a single cell, normalized to the average brightness of the monomeric control β_1AR-EYFP. (*D*) Binned average oligomeric state values from single molecule (filled gray circle) and SpIDA data (open white circles) as a function of receptor number per square micrometer of membrane area, with SD on both axes. A sigmoidal curve (dark gray) fitting yielded the dimer dissociation constant of 33.6 (27.5 to 39.6) receptors per μm^2 (mean and CI). The fitted line saturated at 2.21 (1.97 to 2.39) (mean and CI). The shaded pink area marks the range of oncogenic CXCR4 levels (as observed in refs. 31 and 32). (*E*) Schematics of the dimer dilution SpIDA: SNAP-CXCR4 dimerization with CXCR4-EYFP (*Top Right*, EYFP as yellow ball, SNAP tag as red) results in lower ε than a CXCR4-EYFP homodimer (*Top Left*). Representative images of HEK293AD cells coexpressing CXCR4-EYFP (*Bottom Right*, gray) + SNAP-CXCR4 labeled with SNAP-Surface 647 (*Bottom Right*, red), and CXCR4-EYFP (*Bottom Left*, gray) + empty vector as negative control. (*F*) SpIDA on HEK293AD cells coexpressing β_1AR-EYFP + vehicle (dark gray), β_1AR-EYFP + SNAP-β_1AR (light gray), CXCR4-EYFP + empty vector (yellow) and CXCR4-EYFP + SNAP-CXCR4 (red). The data are displayed with mean ± SD from three independent experiments.

Some fluorescent proteins have been described to self-assemble within cellular compartments (38). Therefore, we tested whether the observed CXCR4-EYFP dimers are a result of EYFP self-assembly or true CXCR4 homointeractions. To do so, we applied a different labeling strategy by using an N-terminal SNAP-tagged CXCR4 (SNAP-CXCR4), labeled with SNAP-Surface Alexa Fluor 488 dye, and performed SpIDA in intact cells. Again, SNAP-β_1AR served as a monomeric control. Also with this label, CXCR4 exhibited an expression-dependent dimerization profile, comparable to that seen with CXCR4-EYFP (*SI Appendix*, Fig. S2*G*). This confirms that the dimeric organization of CXCR4-EYFP is truly mediated by receptor interactions, and not due to nonspecific fluorescent protein interactions.

We also tested whether the density dependence of dimerization could be reproduced in a different cellular context. In agreement with published data (39), we did not detect any endogenous CXCR4 in our in CHO cells with a fluorophore-conjugated antibody (*SI Appendix*, Fig. S3 *C* and *D*). This allowed us to perform SpIDA in intact CHO cells, which were transiently transfected with EYFP-tagged CXCR4. We again observed a concentration-dependent fashion of CXCR4 dimerization (*SI Appendix*, Fig. S2*H*), supporting the data obtained in HEK293AD cells.

CXCR4 dimerization at high density was further confirmed by coexpressing an N-terminally SNAP-tagged CXCR4 with CXCR4-EYFP (Fig. 2*E*). As expected, coexpression of SNAP-CXCR4 resulted in a reduced CXCR4-EYFP dimerization, as evidenced from a decreased EYFP brightness, indicating that the SNAP-tagged CXCR4 competed with CXCR4-EYFP in their dimerization (Fig. 2*F*). In cells cotransfected with CXCR4-EYFP and empty vector, the dimeric CXCR4 behavior remained intact (Fig. 2*F*). As a control for a monomeric behavior, we showed that expressing SNAP-β_1AR with β_1AR-EYFP did not affect β_1AR-EYFP brightness noticeably, as to be expected, given that β_1AR-EYFP exhibits an essentially monomeric distribution (Fig. 2*F*).

Together, these results suggest that CXCR4-EYFP shows density-dependent dimerization, making it at oncogenic expression levels a pure dimer.

Selective Antagonists of CXCR4 Can Disrupt CXCR4 Dimerization with Different Efficacies. We next assessed whether ligands targeting CXCR4 can modify the receptor dimerization. Using SpIDA in intact HEK293AD cells at levels where the CXCR4-EYFP is prevalently dimeric (>50 molecules per μm^2), we first tested the endogenous CXCR4 agonist, CXCL12. Within 1 min, 100 nM CXCL12 did not alter the dimeric stoichiometry substantially (Fig. 3*A*). At later time points, CXCR4-EYFP formed clusters (*SI Appendix*, Fig. S4*A*) that colocalized with clathrin-associated adaptor protein AP2 subunit μ2 (*SI Appendix*, Fig. S4*C*). Temporal kinetics of cluster formation and receptor internalization by CXCL12 were in good correlation (*SI Appendix*, Fig. S4 *D* and *E*) and were preceded by β-arrestin2 recruitment kinetics (*SI Appendix*, Fig. S4*F*).

We then tested antagonists with distinct chemical and structural properties: the bicyclam small-molecule antagonists AMD3100 and AMD3465, the T140 derivative peptide TC14012, the isothiourea derivative small-molecule IT1t, the cyclic peptides LY2510924 and FC131, and the nanobody VUN401 (40). Results with the antagonists displayed distinct profiles: AMD3100 and AMD3465 did not change the basal CXCR4 stoichiometry, and TC14012 induced only a slight decrease (Fig. 3*A* and *SI Appendix*, Fig. S5 *A*–*C* and Table S1). In contrast, LY2510924 and IT1t produced a significant decrease (Fig. 3*A* and *SI Appendix*, Fig. S5 *D* and *E*). Moreover, FC131 and VUN401 disrupted CXCR4-EYFP dimers completely at varying expression ranges (Fig. 3*A* and *SI Appendix*, Fig. S5 *F* and *G* and Table S1).

To understand how fast the new monomeric state can be reached, we then evaluated the kinetics of dimer destabilization induced by FC131 and IT1t using SpIDA. This analysis revealed that dimer destabilization starts within the first 30 s of FC131 treatment and equilibrates to the monomeric state with a tau (τ)-value of 50 s (30 to 84 CI), while IT1t-mediated destabilization occurs with $\tau = 46$ s (30 to 72 CI). The nanobody VUN401 displayed a rapid disruption of dimers, with $\tau = 17$ s (0 to 50 CI) (Fig. 3*B*).

We also tested the dimer disrupting effect of the ligands using a temporal brightness (TB) approach commonly referred to as the number and brightness method (41, 42). The results from this assay accurately reflected those obtained by SpIDA analysis (Fig. 3*C*).

To rule out that our SpIDA-based oligomerization analyses might be influenced by receptor clustering or binding to heterologous interaction partners, which may not be associated with specific receptor–receptor interactions, we performed a careful area selection in our measurements (35). Furthermore, as a conceptually independent control that reports direct protein–-protein interactions at the nanometer scale, we performed fluorescence resonance energy transfer (FRET) acceptor photobleaching (FRET AB). For CXCR4 in its basal state, we observed a hyperbolic increase of FRET efficiency with increasing

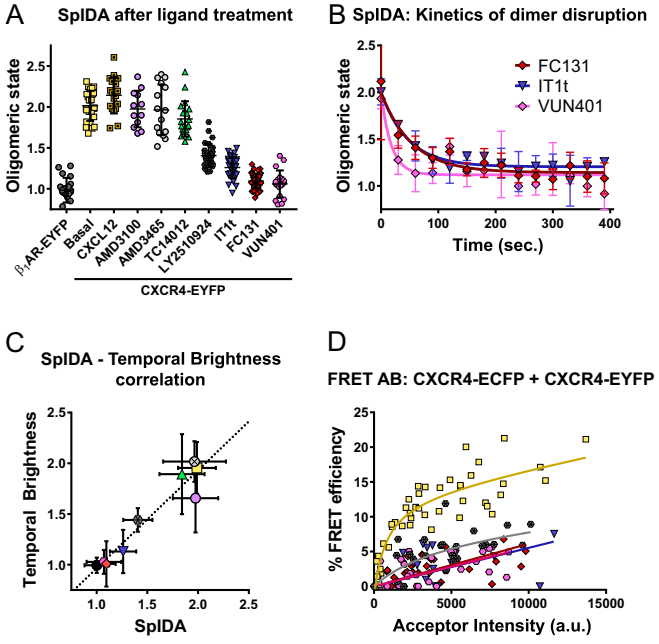

Fig. 3. CXCR4 antagonists modulate receptor dimerization with distinct profiles. (*A*) SpIDA analysis of HEK293AD cells expressing β_1AR-EYFP (dark gray) and CXCR4-EYFP (yellow) and CXCR4-EYFP after 20 min of incubation with ligands: 10 μM AMD3100 (purple), 10 μM AMD3465 (gray), 10 μM TC14012 (green), 100 nM LY2510924 (dark gray), 10 μM IT1t (blue), 10 μM FC131 (red), and 1 μM VUN401 (pink). Each data point represents a brightness value from one cell normalized to the monomer control, given with mean ± SD as error bars. Data were obtained from at least three experiments per condition. Statistical tests and multiple comparisons of conditions are provided in *SI Appendix*, Table S1. (*B*) SpIDA kinetics of dimer destabilization by VUN401, IT1t, and FC131. Different cells were imaged for SpIDA analysis for 20 min at 30-s intervals upon ligand addition. Plotted values over time were fitted to a monoexponential decay function. The data represent mean ± SD of three independent experiments. (*C*) Correlation of average oligomeric states (with SD) obtained from SpIDA (*x* axis) and TB measurements (*y* axis). Color coding of the data points is the same as in *A*. Black straight line is the linear fit of the data (slope: 0.94 [0.873 to 1.014 CI]), representing the degree of correlation for two methods. (*D*) FRET acceptor photobleaching experiment in HEK293AD cells coexpressing CXCR4-ECFP and CXCR4-EYFP. Each data point is obtained from a single cell. Color coding of the data points is the same as in *A*.

EYFP intensity, indicating specific interactions between CXCR4-ECFP and CXCR4-EYFP. In the presence of LY2510924, we also observed a hyperbolic behavior, but with lower FRET efficiency and a lower dissociation constant (K_d =20,587 intensity units, IU) than that for CXCR4 alone (K_d = 700 IU), indicating decreased CXCR4 homodimerization. FC131, IT1t, and VUN401 also reduced FRET efficiencies and resulted in a linear FRET increase (Fig. 3*D*), indicating unspecific receptor−receptor interactions.

Altogether, these results suggest that the CXCR4 dimerization is specific, and that it can be modulated in a ligand-specific manner. LY2510924 binding moderately decreased CXCR4 dimerization, while IT1t, FC131, and VUN401 disrupted it completely, and the average stoichiometry became monomeric in ensemble measurements.

CXCR4 Dimerization Is Linked with Receptor Activity. Having observed that certain antagonists can disrupt CXCR4 dimers, we questioned whether this spatial rearrangement is linked to receptor activity. First, we measured G protein activation by CXCR4, using a FRET-based Gi_2 protein activation biosensor (43), for which a decrease in FRET reports Gi protein activation. With the agonist CXCL12, we observed a 13% decrease in FRET, indicating Gi_2 sensor activation. Compared to the buffer control, AMD3100, AMD3465, and VUN401 did not induce any major FRET change. TC14012 induced a small increase. LY2510924, IT1t, and FC131 produced a much higher increase, pointing out a certain level of basal Gi_2 activation that was significantly reversed by these three ligands (Fig. 4*A* and *SI Appendix*, Table S2). To assess the degree of this basal Gi_2 activity in CXCR4-expressing cells, we treated cells with Pertussis toxin (PTx), an inhibitor of Gi_2 activity. This treatment resulted in a 5% higher FRET signal of the Gi_2 sensor, which indicates the span of the FRET change induced by CXCR4 basal activity (Fig. 4*A*; see also Fig. 6*B*).

Using the same experimental setup, we tested whether these ligands can also modulate G protein signaling triggered by a constitutively active mutant (CAM) of CXCR4, produced by mutating Asp119 to Ser ($N119^{3.35}S$) (44). We detected a lower basal FRET ratio of the Gi_2 sensor with this mutant compared to the wild-type (WT) CXCR4, indicating further constitutive activity of CXCR4 $N119^{3.35}S$ mutant (*SI Appendix*, Fig. S6*A*). With CXCR4 CAM, CXCL12 and AMD3100 further decreased the FRET signal by the Gi_2 sensor. AMD3465 produced a minor increase. TC14012, LY2510924, IT1t, and FC131 induced a significant FRET increase, while VUN401 induced no FRET change (*SI Appendix*, Fig. S6*B* and Table S2). These experiments showed that TC14012 acts as an efficient inverse agonist on the CAM CXCR4, but its effect on the WT receptor is only minor. LY2510924, FC131, and IT1t are inverse agonists of both the WT and the CAM CXCR4, as seen at the G protein level.

To further understand the downstream effects of CXCR4 ligands, we employed a bioluminescence resonance energy transfer (BRET)-based assay in 96-well plate format. We measured interactions between C-terminally nanoluciferase-tagged CXCR4 (CXCR4-nLuc) and C-terminally SYFP tagged $G\gamma_2$ subunit ($G\gamma_2$-SYFP), transfected together with the $G\alpha i_2$ and $G\beta_1$ subunits for proper G protein stoichiometry. With the agonist CXCL12, we observed a concentration-dependent decrease in BRET. In contrast, except AMD3100 and AMD3465, all other ligands exhibited a concentration-dependent increase in BRET (Fig. 4*B*). Surprisingly, despite having no effect on the G protein activity, in the BRET assay, the nanobody VUN401 displayed the largest efficacy and potency among all antagonists (*SI Appendix*, Fig. S6*C*), followed by FC131, LY2510924, and IT1t.

The nanobody displayed its monomerizing effect also on the CAM CXCR4, yet without changing the activity of this mutant, even though FC131 still retained its ability to reduce both constitutive activity and dimerization also in this mutant (*SI Appendix*, Fig. S7).

Overall, there was a clear correlation (R = 0.77) between the effects of the various ligands on G protein activation (as assessed by the Gi_2 sensor) and on the dimerization behavior of the CXCR4 (Fig. 4*C*). Fitting a linear regression resulted in a nearly identical slope (m = 0.011 [0.010 to 0.012 CI]) with a pseudo-correlation (m = 0.010) where we assumed that zero basal activity corresponds to monomeric CXCR4 and 100% basal activity to dimeric receptor. While all small-molecule ligands were almost perfectly placed on the correlation line, the nanobody VUN401 was a clear exception, since it almost completely prevented dimerization but did not affect basal activity (Fig. 4*C*).

Following these observations, we asked whether the presence of the heterotrimeric G protein or β-arrestin contributes to CXCR4 dimerization. We performed SpIDA analysis of CXCR4-EYFP in HEK293 cells in which all genes encoding for functional Gαs, Gαq, GαI, and Gα12/13 proteins (ΔGα HEK293) or β-arrestin1/2 (Δβarr HEK293) are knocked out by genome editing. In these cells, we again observed a dimeric CXCR4 behavior, and FC131, IT1t, and VUN401 were still able to disrupt CXCR4 dimers efficiently (*SI Appendix*, Fig. S8). This indicates that CXCR4 homodimers are stabilized neither by heterotrimeric G proteins nor by β-arrestins.

Distinct Ligand Binding Modes Correlate with Their Dimer Destabilization. Intrigued by the ability of CXCR4 inverse agonists to disrupt dimers and reverse the receptor basal signaling, we asked whether distinct ligand binding modes might explain these newly discovered effects. To understand this, we determined the binding poses of all experimentally tested ligands on the CXCR4 crystal structure (21) based on experimentally validated mutation and structure−activity relationship data from the literature (see *Materials and Methods* for references). As a result, we obtained specific binding poses of all tested ligands (Fig. 5*A*). Our approach showed that the residues on CXCR4 that interact with ligands clustered into the transmembrane major and minor binding pockets (45), and the extracellular domain of CXCR4 (Fig. 5*C*).

In contrast to the distinct extracellular binding of the nanobody VUN401 (Fig. 5*B*) (40), all of the other antagonists interact essentially with the transmembrane binding pocket. Among these, AMD3100 (Fig. 5*D* and *SI Appendix*, Fig. S9*A*), AMD3465 (Fig. 5*E* and *SI Appendix*, Fig. S9*B*), and TC14012 (Fig. 5*F* and *SI Appendix*, Fig. S9*C*) bind exclusively to the major pocket, all specifically interacting with the acidic residues $Asp171^{4.60}$ (TM4) and $Asp262^{6.58}$ (TM6). All ligands that reduce the receptor dimerization and basal activity display a common binding mode that is different from that of AMD3100, AMD3465, and TC14012: IT1t (Fig. 5*H*) was found prevalently in the minor binding pocket, forming interactions with the TM2 residues $Trp94^{2.60}$, $Asp97^{2.63}$, and $Tyr116^{3.32}$ (*SI Appendix*, Fig. S9*E*). FC131 was accommodated between the major and minor pocket (Fig. 5*G*) with its L-Arg^2 residue extending toward the minor pocket (*SI Appendix*, Fig. S9*D*) to form an ionic contact with $Asp97^{2.63}$ (TM2) and a cation−pi interaction with $Tyr116^{3.32}$.

Generation of an experimentally validated binding pose of LY2510924 was not possible, due to a lack of mutation data in the literature to guide and prioritize structural models (compared to the rest of the ligands reported in this manuscript). However, LY2510924 was previously reported to possess an extended binding mode (46); it interacts with residues in the major pocket ($Asp187^{45.51}$, $Arg188^{45.52}$, $Tyr190^{45.54}$, and $Gln200^{5.39}$) and extends toward the minor pocket via interactions with $His113^{3.29}$ and $Glu288^{7.39}$ (*SI Appendix*, Fig. S9*F*).

To test experimentally whether the minor pocket binding indeed plays a role in modulating receptor dimerization, we mutated the minor pocket residue tyrosine (Y) 116 to serine (S) ($Y116^{3.32}S$), as this residue is critical for FC131 and IT1t binding

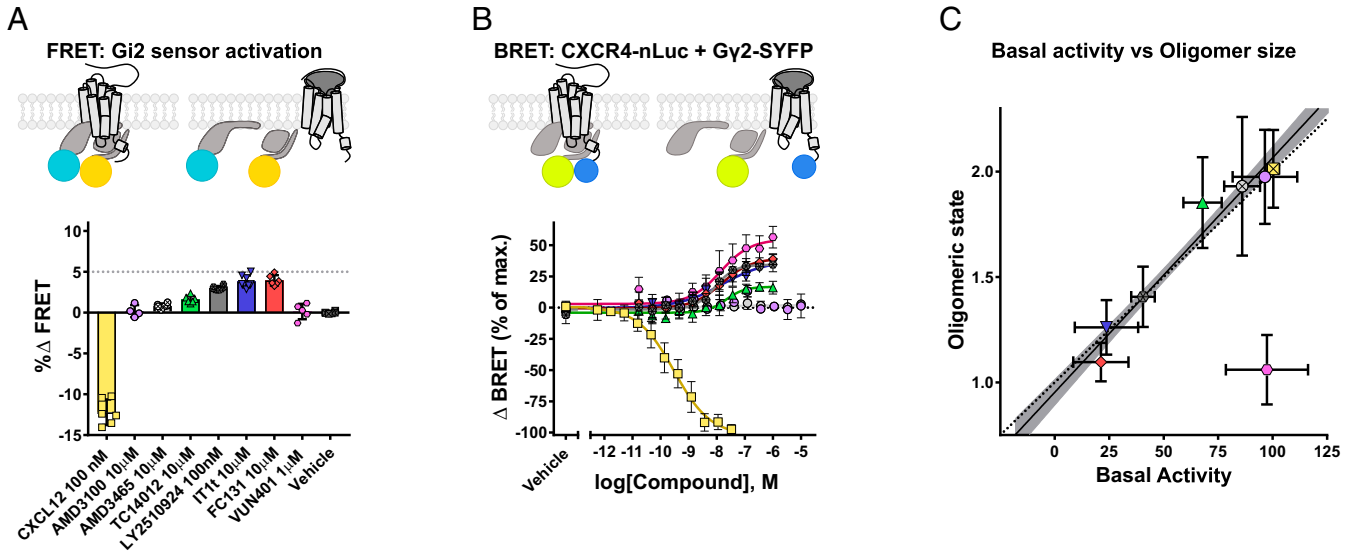

Fig. 4. CXCR4 constitutively activates Gi_2. (*A*) (*Top*) Schematics of the FRET based Gi_2 activation measurement. Gi_2 sensor is in the high FRET conformation at the resting state. CXCL12 binding to CXCR4 induces a lower FRET state of the sensor. (*Bottom*) FRET changes in the Gi_2 sensor by CXCR4 ligands. Scatter dot plots with bars show average FRET changes 20 min after the addition of different ligands. The dotted gray line represents the average ΔFRET resulting from PTx treatment. Error bars represent SD of at least four independent experiments. Statistical significance analysis is provided in *SI Appendix*, Table S2. (*B*) (*Top*) Schematics of the BRET measurement between CXCR4-nLuc and $G\gamma_2$-SYFP. At the basal state, CXCR4-nLuc and $G\gamma_2$-SYFP are at BRET distance. CXCL12 binding to CXCR4-nLuc results in a decrease in BRET. (*Bottom*) Concentration–response curves obtained by fitting the data to a four-parameter Hill equation. Obtained pEC_{50} values: CXCL12: 9.5 (9.7 to 9.3 CI); LY2510924: 8.1 (8.2 to −7.9 CI); TC14012: 7.7 (8.0 to 7.3 CI); IT1t: 7.8 (8.3 to 5.7 CI); VUN401: 7.9 (8.3 to 6.6 CI). Data points at each concentration show the mean ± SD from at least three independent plate reader experiments. (*C*) Correlation plot of basal activity and oligomeric state; oligomeric state values were obtained from the data given with SD error bars in Fig. 3*A*. Basal activity data (with SD error bars) was generated by normalizing the data in *A* to % ΔFRET of PTx (as 0%) and vehicle treatment (as 100%). The dotted line shows the assumed pseudocorrelation, and the black line is the actual fit (VUN401 was identified as an outlier; *SI Appendix*, Table S3) with 95% CI (in gray).

(21, 47). Then, we assessed the oligomeric state of this mutant using SpIDA. At densities above 60 molecules per μm^2 membrane area, $Y116^{3.32}S$ displayed a highly dimeric behavior. While 100 nM IT1t or FC131 were able to disrupt dimerization of WT CXCR4, these ligands were remarkably less efficient in destabilizing the $Y116^{3.32}S$ dimers (*SI Appendix*, Fig. S9*G*).

In conclusion, our docking and experimental data reveal common binding features for the ligands that support their dimer destabilizing ability. While the antagonists that form contacts with minor pocket residues (IT1t, LY2510924, and FC131) are effective in breaking CXCR4 homodimer formation, those that bind entirely to the major pocket do not disrupt these dimers.

TM6 Mutations Attenuate CXCR4 Basal Activity and Dimerization. Having observed that the basally active CXCR4 forms dimers, and that inhibition of basal activity correlates with disruption of dimers, we sought to understand the molecular mechanisms mediating this behavior. We thus focused on the transmembrane residues that control the conformational switch of CXCR4 (48). Among these, the TM6 residues valine (V) $242^{6.38}$ and leucine (L) $246^{6.42}$ reside in the center of the conserved signaling motifs of GPCRs (Fig. 6*A*), and have been proposed to regulate the microswitches that activate CXCR4 (48) via interactions with side chains of TM helices 5, 6, and 7. Therefore, we generated a V242 to aspartate mutant ($V242^{6.38}D$) and L246 to proline ($L246^{6.42}P$) to abolish signaling of CXCR4. The $V242^{6.38}D$ mutation converted CXCR4 from an exclusively dimeric to an exclusively monomeric state (Fig. 6*B*). Moreover, this mutant markedly reduced the basal Gi activity (visible from an increased basal FRET ratio of the Gi_2 sensor) (Fig. 6*C*), and displayed no response to any ligand in the Gi activation assay (*SI Appendix*, Fig. S10*A*). Similarly, $L246^{6.42}P$ also displayed a markedly reduced dimeric behavior (Fig. 6*B*). This mutant also displayed a reduced basal activity on the G protein assay, yet to a lesser extent compared to the $V242^{6.38}D$ mutant. In line with this, the partial basal activity of the $L246^{6.42}P$ mutant was further inhibited by IT1t and FC131 (*SI Appendix*, Fig. S10*B*).

When we compared the extent of basal activity and oligomeric state of these mutants with the WT CXCR4, we again observed a notable positive correlation between the basal activity and receptor stoichiometry of our TM6 mutants ($R = 0.7$), further confirming the relationship between these two features (Fig. 6*D*).

Together, these results demonstrate that the $V242^{6.38}D$ mutation induces a CXCR4 conformation, which no longer activates Gi basally, and is unresponsive to any ligand. In contrast to the WT receptor, this mutant presents an essentially monomeric organization. This supports the importance of basal activity of the CXCR4 for its dimerization. Also, the degree of reduction in the basal activity and dimerization in $L246^{6.42}P$ mutant corroborate the positive correlation between the basal activity and dimerization of CXCR4.

Discussion

Growing evidence indicates that several class A GPCRs can form dimers and oligomers, but the molecular mechanisms that mediate their oligomerization and the downstream effects are poorly understood. Here, we studied the biophysical dynamics and conformational implications of CXCR4 membrane organization at expression levels ranging from ∼200 to ∼100,000 receptors per cell. Cells relevant for physiological CXCR4 functions express from a few thousands to 150,000 copies of CXCR4 (26, 49), while metastatic breast cancer cells express above 100,000 CXCR4 copies per cell (31). At the low expression levels that are required for single-molecule experiments, CXCR4 was found to be mainly monomeric, but individual CXCR4 receptors formed transient homodimers. Their lifetimes were longer than those of μ-opioid (29), M_1 muscarinic (11), and

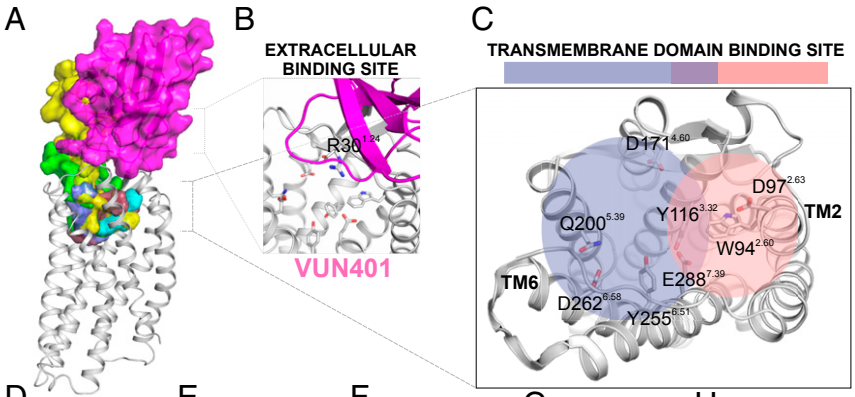

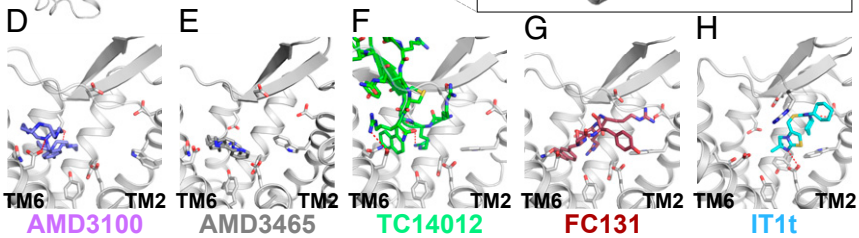

I

Ligand \ Residue	R$^{1.24}$	D$^{4.60}$	Q$^{5.39}$	Y$^{6.51}$	D$^{6.58}$	Y$^{3.32}$	E$^{7.39}$	W$^{2.60}$	D$^{2.63}$
AMD3100		■			■		■		
AMD3465		■			■		■		
TC14012		■	■		■				
IT1t						■	■	■	■
FC131		■		■		■			■
VUN401	■								

Fig. 5. Binding modes of different CXCR4 ligands are connected with their ability for dimer destabilization. (*A*) Overview of the CXCR4 crystal structure (PDB ID code 3OE0, gray cartoon) with docked VUN401 (magenta), TC14012 (green), AMD3100 (purple), FC131 (brown), CXCL12 (yellow), and IT1t (cyan), seen detailed in *B* and *D*–*G*. Ligand docking was based on the data displayed in *SI Appendix*, Fig. S9. (*B*) Zoom-in view of the transmembrane domain binding site of CXCR4, where no VUN401 interactions are observed. VUN401 binds in view of the extracellular vestibule of CXCR4 and its epitope has been matched to the residue R30 in the CXCR4 N terminus. (*C*) Top view of the CXCR4 transmembrane domain binding site, which can be divided into a minor pocket comprising TM1-3 and TM7 (rose), and a major pocket, comprising TM3-7 (purple). The side chains of residues that have been experimentally validated to interact with CXCR4 ligands are presented in sticks in all binding mode representations. (*D*–*H*) Binding mode representations based on literature data of (*D*) AMD3100, (*E*) AMD3465, (*F*) TC14012 (based on cocrystallized ligand CVX-15), (*G*) FC131, and (*H*) IT1t. Images were placed from left to right to visualize the binding pose shift from major to minor pocket. (*I*) Overview of the CXCR4 residues that are in contact with ligands. (For references, see *Materials and Methods*.) Individual residue–ligand atomic interactions are summarized in *SI Appendix*, Fig. S9.

D_2 dopamine receptors (50), but in agreement with those of the neurotensin 1 receptor (NT1R), which exhibits a dynamic and density-dependent dimerization (51). Much like the NT1R, CXCR4 homodimers also became prevalent with increasing receptor expression. However, the essentially fully dimeric nature of CXCR4 at higher expression levels suggests the existence of dimers with far longer half-lives than can be observed in single particle tracks, as has been suggested for agonist-stimulated μ-opioid receptor dimers (29). The highly dimeric nature of CXCR4 at densities >50,000 receptors per cell (>70 receptors per μm^2 membrane) might as well represent the scenario of CXCR4 organization in oncogenic cells. Yet, it should be noted that CXCR4 is expressed in diverse tissues, and the receptor's membrane organization may be significantly influenced by different cellular contexts and the abundance of interaction partners (52).

Agonist (CXCL12) stimulation apparently further induces dimerization, but this is difficult to differentiate from subsequent agonist-induced clustering that leads to CXCR4 internalization. We observed that CXCR4 remains dimeric within 1 min after agonist-mediated activation. This supports our recent observation of a rapid dimeric rearrangement upon activation, rather than a shift in oligomer stoichiometry (53). Moreover, the dimeric stoichiometry of CXCR4 within the time that is needed for full G protein activation (53) also suggests that the agonist-bound CXCR4 dimer is conformationally distinct from the basal dimers.

The dimeric CXCR4 nature appears to be closely linked to its known basal activity (53, 54). In contrast to AMD3100 and AMD3465, that are exclusive major pocket binders, LY251092, IT1t, and FC131, ligands that bind entirely or partially the minor pocket of CXCR4, efficiently reduced basal activity and also disrupted receptor homodimers. Furthermore, the slight inverse agonism of TC14012 correlates with its lack of efficiency in disrupting CXCR4 dimers. Thus, minor pocket ligands, which presumably affect critical residues that are required to initiate CXCR4 signaling (48), inhibit both basal activity and dimer formation. The decreased dimer disruption abilities of FC131 and IT1t in the Y116$^{3.32}$S mutant support the importance of minor pocket binding to modulate receptor dimerization. Altogether, we observed a positive correlation between CXCR4 basal activity and dimeric organization. In line with this, the CXCR4 V242$^{6.38}$D mutant which exhibits virtually no basal activity is monomeric, supporting the notion that the basally active receptor conformation essentially mediates dimerization. Moreover, low basal activity and decreased dimeric organization of the L246$^{6.42}$P mutant also supports that the degree of basal activity determines the degree of CXCR4 dimerization. CXCR4 dimerization in the absence of functional G proteins or of β-arrestin1/2 corroborates that the dimerization is an intrinsic

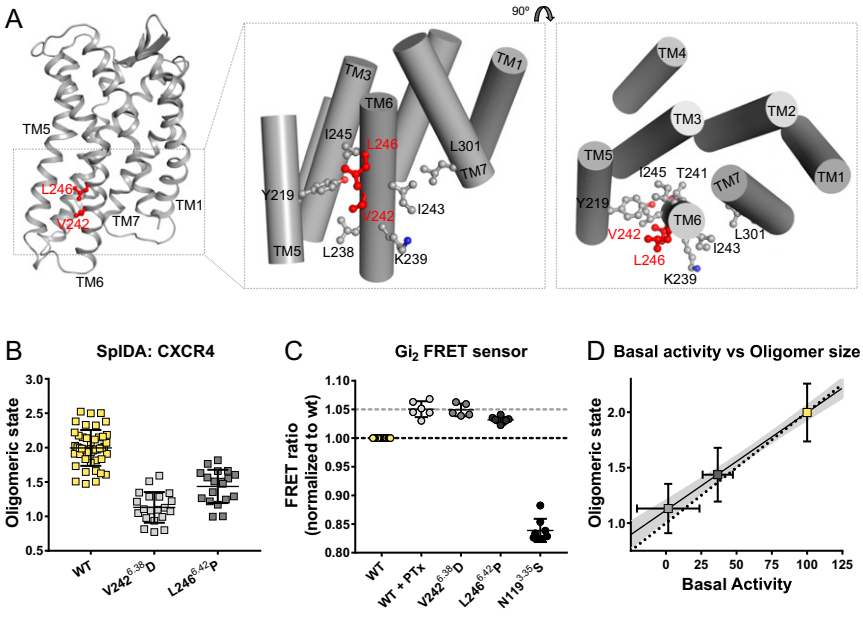

Fig. 6. CXCR4 V242$^{6.38}$D and the L246$^{6.42}$P mutants are monomeric and display no basal or ligand-induced activity. (*A*) (*Left*) Position of the V242$^{6.38}$ residue on CXCR4 model (68). V242$^{6.38}$ interacts with other TM6 residues (shown as sticks) and forms a hydrophobic network that stabilizes the microswitch residues on TM5 and TM7 (shown as sticks), viewed from side (*Middle*) and top (*Right*). (*B*) SpIDA shows that the V242$^{6.38}$D mutant (light gray) is mainly monomeric and the L246$^{6.42}$P is largely monomeric in comparison to the WT CXCR4 (yellow). (*C*) V242$^{6.38}$D and L246$^{6.42}$P mutants display higher basal FRET ratios (lower basal G protein activity), in comparison to the WT CXCR4 (yellow) on FRET-based Gi_2 sensor. PTx-induced increase in FRET probes the basal activity of CXCR4. (*D*) Correlation plot of basal activity and oligomeric state for the TM6 mutants; data with SD error bars were derived from *B* and *C*. The dotted line indicates the pseudocorrelation. The black line with 95% CI (gray shades) is the actual fit (slope m = 0.009 [0.008 to 0.010 CI]).

feature of basal as well as agonist-induced active receptor conformations. This is in line with the recent observations that class A GPCRs can adopt an active conformation and display intrinsic activity even in the absence of G proteins (55–57).

In contrast, if dimerization is prevented by a steric hindrance by the use of the nanobody VUN401, which binds to the extracellular domains of CXCR4 and does not reach the major or minor subpockets, the receptor activity is not affected. This indicates that mechanical disruption of CXCR4 dimerization alone does not translate into changes in activity. Therefore, CXCR4 dimerization is a consequence of its basal activity, and inhibition of CXCR4 basal activity leads to dimer disruption.

Moreover, the observation that the nanobody VUN401 does not affect basal activity, yet alters the interaction between CXCR4 and G proteins (as evidenced from the CXCR4/Gγ_2 BRET assay), implies that there may be different ways CXCR4 dimers and monomers interact with G proteins that result in similar extents of basal activity.

Developing efficacious CXCR4 antagonists is of major clinical interest (14). Ligands targeting the minor pocket of CXCR4 (58) or diminishing the CXCR4 basal activity have been reported to effectively reverse inflammation in vivo (59). This highlights how the binding mode and signaling outcome of CXCR4 ligands may determine their effectiveness in pathologies. Therefore, it would be interesting to further clinically evaluate those CXCR4 ligands that specifically bind to the minor pocket, act as inverse agonists, and disrupt receptor dimers. The common binding motifs in the minor pocket observed for the dimer-destabilizing ligands may, thus, serve as a scaffold to develop more potent and efficient inhibitors of CXCR4 activity as well as dimerization.

Materials and Methods

Materials. AMD3100 was purchased from Sigma-Aldrich. AMD3465, TC14012, and FC131 were from Tocris Bioscience. LY2510924 was from MedChemExpress. Human recombinant CXCL12 was from Peprotech. SNAP-Surface 549, SNAP-Surface Alexa Fluor 488, and SNAP-Surface Alexa Fluor 647 were purchased from New England Biosciences. Alexa Fluor 488 conjugated CXCR4 antibody (#44717, FAB173G) was purchased from R&D Systems.

Molecular Biology. The CXCR4 complementary DNA (cDNA) sequence was provided in pcDEF3 vector plasmid through the Oncogenic GPCR Network of Excellence and Training (ONCORNET) consortium from Vrije Universiteit Amsterdam. In order to generate a CXCR4-encoding pcDNA3 expression construct, the CXCR4 sequence was digested from the pcDEF3 construct using the restriction enzymes EcoRI and XbaI and ligated into pcDNA3 vector that was digested using the same restriction enzymes. To generate pcDNA3-SNAP-CXCR4 expression construct, the CXCR4 sequence was PCR amplified using the primers 5′-CTAGCTAGCGATGAGGGGATCAGTATATA-3′ (forward) and 5′-CCCTCGAGTTAGCTGGAGTGAAAACTTGAA-3′ (reverse) and digested using the restriction enzymes NheI and XhoI. The digested fragment was ligated in frame with a SNAP encoding sequence in the previously described pcDNA3-SNAP construct. To generate pcDNA-CXCR4-EYFP expression construct, the CXCR4 encoding sequence was PCR amplified using the following primers: 5′-AAAGAATTCATGGAGGGGATCAGTATATACAC-3′ (forward) and 5′-AAATCTAGAGCTGGAGTGAAAACTTGAAGA-3′, and the amplified fragment was digested using the restriction enzymes EcoRI and XbaI, and then subsequently cloned in a previously described pcDNA3-beta2AR-EYFP construct in frame with EYFP encoding sequence. To generate pcDNA-CXCR4-nLuc expression construct, nLuc encoding sequence (purchased from Promega) was PCR amplified 5′-AAATCTAGA GTCTTCACACTC-GAAGATTTCGTTGGGGAC-3′ (forward) and 5′-AAAGCGGCCGC TTACGCCAG-AATGCGTTCGCACAG-3′ (reverse) and digested using the restriction enzymes XbaI and NotI. The digested nLuc fragment was ligated in the pcDNA3-CXCR4-EYFP construct, replacing EYFP. Y116$^{3.35}$S, N119$^{3.35}$S, V242$^{6.38}$D, and L246$^{6.42}$P mutants were generated using the Q5 Site-Directed Mutagenesis Kit (New England Biomedicine) with the following primers: 5′-CCATGTCAT-CTCCACAGTCAACC-3′ and 5′- ACTGCCTTGCATAGGAAG-3′ (Y116$^{3.35}$S); 5′-CTACACAGTCtctCTCTACAGCAGTG-3′ and 5′-ATGACATGGACTGCCTTG-3′ (N119$^{3.35}$S); 5′-CAAGACCACAgacATCCTCATCCTGG-3′ and 5′-AGGGCCTTG-CGCTTCTGG-3′ (V242$^{6.38}$D); 5′-CATCCTCATCCCAGCTTTCTTCGCCTG-3′ and 5′-ACTGTGGTCTTGAGGGCC-3′ (L246$^{6.42}$P).

Gi_2 sensor (pGβ1-2A-cp173Venus-Gγ2-IRES-Gαi2-mTurquoise2Δ9) was a gift from Dorus Gadella, University of Amsterdam, Amsterdam, the Netherlands (Addgene plasmid #69624). AP2μ2-mCherry was a gift from Christien Merrifield, Université Paris-Saclay, Paris, France (Addgene plasmid #27672).

Cell Culture. HEK293AD cells (BioCat) were cultured in Dulbecco's modified Eagle's medium (DMEM) (PAN Biotech) supplemented with 10% (vol/vol) fetal bovine serum (FBS) (Biochrom AG), 1% L-glutamine (PAN Biotech), penicillin (100 U/mL), and streptomycin (100 μg/mL) at 37 °C and 5% CO_2. CHO cells (ATCC CCL-61) were cultured in phenol red-free DMEM/F12 (Gibco) supplemented with 10% FBS (Biochrom AG), 1% L-glutamine (PAN Biotech), 100 U/mL penicillin, and 100 μg/mL streptomycin at 37 °C and 5% CO_2. To passage cells, medium was aspirated, and cells were washed once with 5 mL of phosphate-buffered saline (PBS) (Sigma-Aldrich), followed by a second wash with trypsin 0.05%/(ethylenedinitrilo)tetraacetic acid 0.02% in PBS for 1 min, then resuspended in DMEM (for HEK293AD cells) or DMEM/F12 (for CHO-K1 cells).

TIRFM Imaging. For single-molecule imaging experiments, CHO-K1 cells were grown on glass coverslips in six-well plates 24 h prior to transfection. Cells were transfected with 2 μg of SNAP-tag incorporated receptor vector using Lipofectamine 2000 (Thermo Fisher Scientific) as previously described (28) and incubated for 4 h to 6 h at 37 °C and 5% CO_2. Transfected cells were labeled using 1 μM SNAP-Surface 549 dye in complete DMEM/F12 medium for 20 min. Cells were then washed three times with 5-min incubation in complete culture medium after each wash. Coverslips with labeled cells were placed in an Attofluor cell chamber (Thermo Fisher Scientific) and supplemented with Hank's Buffered Saline Solution (HBSS). TIRF imaging was performed using a commercial TIRF illuminated Nikon Eclipse Ti2 inverted microscope (Nikon) equipped with a beam splitter connected to four separate electron multiplying-charge coupled device (EM-CCD) cameras (Andor iXon Ultra897), a CFI Apochromat 100× 1.49 TIRF objective with automated correction collar, a laser box with four laser diode lines (405, 488, 561, and 647 nm) coupled through an automated module, and an automated infrared-guided autofocus system. Imaging was performed at constant 20 °C ambient and objective temperature, with continuously active autofocus module. Single TIRF images for intensity analysis were captured with 40-ms acquisition time at 100% laser power. To determine dimerization kinetics, laser illumination was focused to the center of the imaging field by 2× via Nikon-Stochastic Optical Reconstruction Microscopy (N-STORM) module, and 400 to 800 consecutive TIRF images were acquired with 10- to 50-ms time intervals at 100% laser power.

TIRFM Image Analysis and Single-Particle Tracking. Prior to analysis, TIRFM single images and image series were cropped using ImageJ software. Single-particle analysis and tracking was performed using u-track software (60) in MATLAB. Spot intensity data were fetched from the analysis files and plotted in GraphPad Prism and OriginPro. For multi-Gaussian fitting to calculate different oligomer fractions, the mono-Gaussian distribution properties (peak value and full-width at half maximum) of a monomeric control and its increments (2× for dimer, 4× for tetramer) were used as constrained values. Dimerization kinetics was analyzed implementing the track analysis file (from u-track analysis) into Polytracker (publicly available at https://github.com/Blosberg/polytracker) in MATLAB. Collected interaction times were plotted in GraphPad Prism. A two exponential decay function with a fixed τ-value (112 ms) for the fast component was employed to obtain the τ-value and its 95% CIs.

SpIDA. For SpIDA analysis, 3×10^5 HEK293AD cells seeded on clean glass coverslips in six-well plates were transfected with 500 ng of vector plasmid for 16 h to 24 h using Effectene transfection reagent (Qiagen) according to the manufacturer's protocol. For SNAP-tag incorporated receptors, labeling was performed as in TIRFM experiments using SNAP-Surface Alexa Fluor 488 dye. Coverslips with transfected cells were placed in an Attofluor cell chamber (Thermo Fisher Scientific) and supplemented with imaging buffer (HBSS) supplemented with 0.1% (wt/vol) bovine serum albumin (BSA) (Sigma-Aldrich). SpIDA imaging was performed using a commercial laser-scanning confocal microscope (Leica SP8) equipped with a 40×/1.25 NA oil immersion objective, a white light laser (WLL), and photon counting hybrid detectors; 488- and 514-nm lines of the WLL were used for excitation, and emission bands of 500 nm to 650 nm and 520 nm to 600 nm were used for detection of SNAP-Surface Alexa 488 and EYFP, respectively. Images were acquired with 10% laser power with a pixel dwell time of 4.88 μs. Image format was xy, and image size was set to 512 × 512 pixels with 50-nm pixel size. For ligand treatments, cells were supplemented in imaging chamber with imaging buffer + corresponding ligand, and then incubated for 20 min prior to imaging. For time course SpIDA imaging, as soon as ligand was added, different cells were imaged with 30-s intervals. Image analysis was performed using the one-population mode of the SpIDA function using a custom-written MATLAB routine, as described previously (34). Calculated quantal brightness values are real photon counts per fluorescent molecule per pixel dwell time. Polygonal region of interest (ROI) selection was implemented to the MATLAB routine to avoid areas with inhomogeneous fluorescence distribution (i.e., membrane ruffles, clusters).

TB Analysis. For TB analysis, the same imaging setup was used as for SpIDA measurements. The imaging mode was xyt, and 100 frames were taken with a pixel dwell time of 2.43 μs, pixel size of 50 nm, and image resolution 256 × 256 pixels. EYFP-tagged constructs were imaged using a 514-nm line of the WLL with a laser power of 0.75%, and the Hybrid detector was set between 520 nm and 600 nm. Data were analyzed using a custom-written Igor Pro routine as described previously (61), incorporating a boxcar average filtering (62). The brightness values were calculated based on the average of the brightness values from each pixel within the ROI.

FRET AB Imaging. HEK293AD cells were seeded on glass coverslips and transfected identically to the SpIDA experiments. Cell were transfected with CXCR4-EYFP and 250 ng of CXCR4-ECFP together in each well. FRET AB imaging was performed using a commercial Leica TCS SP8 confocal laser-scanning microscope, using the FRET AB module. Image size was 512 × 512 pixels with 50-nm pixel size and 4.88-μs pixel dwell time. Donor and acceptor were imaged at the bottom cell membrane (to visualize and avoid potential heterogeneities on the membrane) using a 405-nm laser at 1% laser power for ECFP excitation, and emission was detected within a wavelength window of 450 nm to 490 nm. For EYFP excitation, the 514-nm laser line of the WLL was used at 1%, and emission was detected between 520 nm and 600 nm. Photomultiplier tube (PMT)-based detectors (with 700-V gain) were used for emission reading. EYFP photobleaching was performed by acquiring 10 images with the 514-nm laser line at 50% laser power. Inhomogeneous areas of the cells were carefully excluded during ROI selection.

CXCR4 Immunostaining. HEK293AD and CHO cells were seeded on glass coverslips in six-well plates and transfected with CXCR4-ECFP or β_1AR-ECFP; 24 h after transfection, cells were washed three times with PBS, and then PBS was replaced with 1% BSA in FluoroBrite medium (Gibco). After 1 h incubation at 37 °C and 5% CO_2, cells were washed three times with PBS and were further incubated at 37 °C and 5% CO_2 with 20 μg/mL human CXCR4 Alexa Fluor 488-conjugated antibody (FAB173G, R&D Systems) in FluoroBrite medium supplemented with 1% BSA; 1 h after incubation, cells were washed three times with PBS and incubated in FluoroBrite medium supplemented with 1% BSA for 3 × 10 min. After the last incubation, cells were imaged with a Leica TCS SP8 confocal laser-scanning microscope. CFP was excited using a 405-nm diode laser at 10% power and detected within the emission window of 430 nm to 490 nm. Alexa Fluor 488 was excited using the 492-nm laser line of the WLL at 10% power, and detected within the emission window of 500 nm to 650 nm. Image size was 512 × 512 pixels with 50-nm pixel size and 4.88-μs pixel dwell time.

BRET-Based Receptor−Gγ Interaction Assay. HEK293AD cells were seeded in 10-cm cell culture dishes at a density of 2×10^6 cells and transfected 24 h after seeding with 500 ng of CXCR4-nanoLuc, 800 ng of $G\alpha i_2$, 500 ng of $G\beta_1$, and 200 ng of $G\gamma_2$-SYFP constructs using Effectene transfection reagent (Qiagen) according to the manufacturer's protocol; 24 h after transfection, cells were transferred into a white-walled, white-bottom 96-well plate, at a density of 10^5 cells per well; 16 h to 24 h after reseeding, medium was removed, cells were washed with PBS and then supplemented with 90 μL HBSS containing furimazine (Promega) (1:1,000 vol/vol). After 10-min incubation at 37 °C, measurement was performed at 37 °C using a Synergy Neo2 Plate Reader (Biotek) using BRET2 filter set. Delta (Δ) BRET for each well was calculated according to the formula

$$\%\Delta\text{BRET} = \left(\frac{\text{BRET}_{\text{post}} - \text{BRET}_{\text{pre}}}{\text{BRET}_{\text{pre}}}\right) \times 100,$$

where $\text{BRET}_{\text{post}}$ is the average BRET ratio values of poststimulus, and BRET_{pre} is the average BRET ratio values measured prestimulus. In each 96-well plate, maximum % ΔBRET observed for CXCL12 stimulus is defined as −100%, and every other % ΔBRET value is then normalized to this.

BRET-Based Receptor−β-Arrestin Interaction and Internalization Assays. HEK293AD cells were seeded in 10-cm cell culture dishes at a density of 2×10^6. For arrestin recruitment assay, cells were cotransfected with 1000 ng of CXCR4-nLuc and 1,000 ng of human β-arrestin2-HaloTag. For internalization assay, a plasmid construct bearing two HaloTags, separated by a repetitive rigid linker, and an N-terminal Lyn-derived sequence (GCIKSKRKDK)

and a C-terminal farnesylation sequence (KKKSKTKCVIM) for plasma membrane localization was used. Then 1,500 ng of this plasmid was cotransfected with 500 ng of CXCR4-nLuc 24 h after seeding, and the cells were transferred into a while-walled, white-bottom 96-well plate, at a density of 10^5 cells per well, and cells were labeled for at least 16 h with HaloTag 618 Ligand (Promega); 16 h to 24 h after reseeding, medium was removed, and cells were washed with PBS and then supplemented with 90 μL HBSS containing furimazine (Promega) (1:1,000 vol/vol). After 10 min incubation at 37 °C, measurement was performed at 37 °C using a Synergy Neo2 Plate Reader (Biotek) using the NanoBRET filter set.

FRET-Based Gi_2 Protein Activation Assay. HEK293AD cells were seeded in 10-cm cell culture dishes at a density of 2×10^6. Cells were cotransfected with 500 ng of CXCR4 and 1,500 ng of Gi_2 FRET sensor 24 h after seeding, as described in previous sections; 24 h after transfection, cells were trypsinized and transferred into a black-walled, black-bottom 96-well plate, at a density of 10^5 cells per well; 16 h to 24 h later, cells were washed with prewarmed PBS, and then 90 μL of prewarmed HBSS was added to each well. After 10-min incubation at 37 °C, measurement was performed at 37 °C using a Synergy Neo2 Plate Reader (Biotek) using a CFP/YFP FRET filter set. After basal FRET measurement, 10 μL of decreasing concentrations of ligands were added to the wells, and FRET ratio was measured again. Delta FRET for each well was calculated according to the formula

$$\%\Delta\text{FRET} = \left(\frac{\text{FRET}_{\text{post}} - \text{FRET}_{\text{pre}}}{\text{FRET}_{\text{pre}}}\right) \times 100,$$

where $\text{FRET}_{\text{post}}$ is the average FRET ratio values of poststimulus, and FRET_{pre} is the average FRET ratio values measured prestimulus.

CXCR4 Ligand Docking. CXCR4 ligand binding modes were obtained with different methods. VUN401 was docked in the CXCR4 crystal structure with Protein Data Bank (PDB) ID code 3ODU (21) using High Ambiguity Driven Biomolecular Docking (HADDOCK) (63) and incorporating the experimentally validated interacting residue Arg30 (40) as active residue for guiding the docking. The T140-derivative peptide TC14012 was modeled based on the CVX15 crystallized structure (PDB ID code 3OE0) (21) from which the last two residues were deleted. AMD3100, AMD3465, and FC131 were docked using the induced-fit docking program of Schrödinger. Residues known from literature to be key for the binding of these ligands were used as restraints: for FC131, residues Asp97, Asp171, and Tyr255 were used (47, 64); for AMD3100 and AMD3465, residues Asp171, Asp262, and Glu288 were used (45, 65–67). IT1t binding mode was directly extracted from the crystal structure (PDB ID code 3ODU) (21). The CXCL12:CXCR4 complex was extracted from a recently published model (68).

Quantification and Statistical Analysis. In scatter dot plots, where average oligomeric sizes are compared, an ordinary one-way ANOVA test in Graphpad Prism was used with Tukey's multiple comparison test, including no matching or pairing. For Figs. 3*A* and 4*A* and *SI Appendix*, Fig. S6*B*, a complete table of statistical significance analysis is provided in *SI Appendix*. In text, statistical significance is referred to a P value < 0.001 from Tukey's multiple comparison test. Statistical analysis of the basal Gi_2 sensor FRET ratios (Fig. 6*C* and *SI Appendix*, Fig. S6*A*) was performed using a paired t test using GraphPad Prism. Outlier analysis on the Fig. 4*C* was done by using robust regression followed by outlier identification (ROUT) method choosing the false discovery rate (Q) as 1.

Data Availability. All study data are included in the article and *SI Appendix*.

ACKNOWLEDGMENTS. This research was funded by European Union's Horizon2020 Marie Skłodowska-Curie Actions (MSCA) Program under Grant Agreement 641833 (ONCORNET) and European Cooperation in Science and Technology (COST) Action CA18133 European Research Network on Signal Transduction (ERNEST). A. Inoue was funded by the Leading Advanced Projects for Medical Innovation (LEAP) JP19gm0010004 from the Japan Agency for Medical Research and Development. We thank all colleagues from ONCORNET for helpful scientific discussions. We thank Francesca Deflorian (Sosei Heptares) for her support with CXCR4 docking studies.

1. K. L. Pierce, R. T. Premont, R. J. Lefkowitz, Seven-transmembrane receptors. *Nat. Rev. Mol. Cell Biol.* **3**, 639–650 (2002).
2. S. Ferré *et al*., G protein-coupled receptor oligomerization revisited: Functional and pharmacological perspectives. *Pharmacol. Rev.* **66**, 413–434 (2014).
3. J. P. Pin, T. Galvez, L. Prézeau, Evolution, structure, and activation mechanism of family 3/C G-protein-coupled receptors. *Pharmacol. Ther.* **98**, 325–354 (2003).
4. E. O. Grushevskyi *et al*., Stepwise activation of a class C GPCR begins with millisecond dimer rearrangement. *Proc. Natl. Acad. Sci. U.S.A.* **116**, 10150–10155 (2019).
5. A. Koehl *et al*., Structural insights into the activation of metabotropic glutamate receptors. *Nature* **566**, 79–84 (2019).
6. M. R. Whorton *et al*., A monomeric G protein-coupled receptor isolated in a high-density lipoprotein particle efficiently activates its G protein. *Proc. Natl. Acad. Sci. U.S.A.* **104**, 7682–7687 (2007).
7. A. Rivero-Müller *et al*., Rescue of defective G protein-coupled receptor function in vivo by intermolecular cooperation. *Proc. Natl. Acad. Sci. U.S.A.* **107**, 2319–2324 (2010).
8. L. Albizu *et al*., Time-resolved FRET between GPCR ligands reveals oligomers in native tissues. *Nat. Chem. Biol.* **6**, 587–594 (2010).
9. S. Dorsch, K. N. Klotz, S. Engelhardt, M. J. Lohse, M. Bünemann, Analysis of receptor oligomerization by FRAP microscopy. *Nat. Methods* **6**, 225–230 (2009).
10. J. M. Fonseca, N. A. Lambert, Instability of a class a G protein-coupled receptor oligomer interface. *Mol. Pharmacol.* **75**, 1296–1299 (2009).
11. J. A. Hern *et al*., Formation and dissociation of M1 muscarinic receptor dimers seen by total internal reflection fluorescence imaging of single molecules. *Proc. Natl. Acad. Sci. U.S.A.* **107**, 2693–2698 (2010).
12. D. Calebiro *et al*., Single-molecule analysis of fluorescently labeled G-protein-coupled receptors reveals complexes with distinct dynamics and organization. *Proc. Natl. Acad. Sci. U.S.A.* **110**, 743–748 (2013).
13. D. J. Scholten *et al*., Pharmacological modulation of chemokine receptor function. *Br. J. Pharmacol.* **165**, 1617–1643 (2012).
14. I. Adlere *et al*., Modulators of CXCR4 and CXCR7/ACKR3 function. *Mol. Pharmacol.* **96**, 737–752 (2019).
15. B. Debnath, S. Xu, F. Grande, A. Garofalo, N. Neamati, Small molecule inhibitors of CXCR4. *Theranostics* **3**, 47–75 (2013).
16. B. Stephens, T. M. Handel, Chemokine receptor oligomerization and allostery. *Prog. Mol. Biol. Transl. Sci.* **115**, 375–420. (2013).
17. J. Lao *et al*., Single-molecule imaging demonstrates ligand regulation of the oligomeric status of CXCR4 in living cells. *J. Phys. Chem. B* **121**, 1466–1474 (2017).
18. Y. Percherancier *et al*., Bioluminescence resonance energy transfer reveals ligand-induced conformational changes in CXCR4 homo- and heterodimers. *J. Biol. Chem.* **280**, 9895–9903 (2005).
19. L. Martínez-Muñoz *et al*., Separating actin-dependent chemokine receptor nanoclustering from dimerization indicates a role for clustering in CXCR4 signaling and function. *Mol. Cell* **70**, 106–119.e10 (2018).
20. J. Wang, L. He, C. A. Combs, G. Roderiquez, M. A. Norcross, Dimerization of CXCR4 in living malignant cells: Control of cell migration by a synthetic peptide that reduces homologous CXCR4 interactions. *Mol. Cancer Ther.* **5**, 2474–2483 (2006).
21. B. Wu *et al*., Structures of the CXCR4 chemokine GPCR with small-molecule and cyclic peptide antagonists. *Science* **330**, 1066–1071 (2010).
22. L. Qin *et al*., Structural biology. Crystal structure of the chemokine receptor CXCR4 in complex with a viral chemokine. *Science* **347**, 1117–1122 (2015).
23. I. Kufareva *et al*., Stoichiometry and geometry of the CXC chemokine receptor 4 complex with CXC ligand 12: Molecular modeling and experimental validation. *Proc. Natl. Acad. Sci. U.S.A.* **111**, E5363–E5372 (2014).
24. S. Armando *et al*., The chemokine CXC4 and CC2 receptors form homo- and heterooligomers that can engage their signaling G-protein effectors and βarrestin. *FASEB J.* **28**, 4509–4523 (2014).
25. V. Morath *et al*., Semi-automatic determination of cell surface areas used in systems biology. *Front. Biosci. (Elite Ed.)* **5**, 533–545 (2013).
26. H. Ueda *et al*., HIV-1 envelope gp41 is a potent inhibitor of chemoattractant receptor expression and function in monocytes. *J. Clin. Invest.* **102**, 804–812 (1998).
27. J. Hesselgesser *et al*., Identification and characterization of the CXCR4 chemokine receptor in human T cell lines: Ligand binding, biological activity, and HIV-1 infectivity. *J. Immunol.* **160**, 877–883 (1998).
28. T. Sungkaworn *et al*., Single-molecule imaging reveals receptor-G protein interactions at cell surface hot spots. *Nature* **550**, 543–547 (2017).
29. J. Möller *et al*., Single-molecule analysis reveals agonist-specific dimer formation of μ-opioid receptors. *Nat. Chem. Biol.* **16**, 946–954 (2020).
30. X. Pan, C. Dalm, R. H. Wijffels, D. E. Martens, Metabolic characterization of a CHO cell size increase phase in fed-batch cultures. *Appl. Microbiol. Biotechnol.* **101**, 8101–8113 (2017).
31. P. Guo, J. O. You, J. Yang, M. A. Moses, D. T. Auguste, Using breast cancer cell CXCR4 surface expression to predict liposome binding and cytotoxicity. *Biomaterials* **33**, 8104–8110 (2012).
32. B. Wang, P. Guo, D. T. Auguste, Mapping the CXCR4 receptor on breast cancer cells. *Biomaterials* **57**, 161–168 (2015).
33. A. G. Godin *et al*., Revealing protein oligomerization and densities in situ using spatial intensity distribution analysis. *Proc. Natl. Acad. Sci. U.S.A.* **108**, 7010–7015 (2011).
34. A. Isbilir *et al*., Visualization of class A GPCR oligomerization by image-based fluorescence fluctuation spectroscopy. bioRxiv:10.1101/240903 (29 December 2017).
35. P. Annibale, M. J. Lohse, Spatial heterogeneity in molecular brightness. *Nat. Methods* **17**, 273–275 (2020).

36. H. Ueda *et al*., Chemically synthesized SDF-1α analogue, N33A, is a potent chemotactic agent for CXCR4/Fusin/LESTR-expressing human leukocytes. *J. Biol. Chem.* **272**, 24966–24970 (1997).
37. A. Blumlein, N. Williams, J. J. McManus, The mechanical properties of individual cell spheroids. *Sci. Rep.* **7**, 7346 (2017).
38. P. J. Cranfill *et al*., Quantitative assessment of fluorescent proteins. *Nat. Methods* **13**, 557–562 (2016).
39. V. Bobkov *et al*., Nanobody-Fc constructs targeting chemokine receptor CXCR4 potently inhibit signaling and CXCR4-mediated HIV-entry and induce antibody effector functions. *Biochem. Pharmacol.* **158**, 413–424 (2018).
40. A. Van Hout *et al*., CXCR4-targeting nanobodies differentially inhibit CXCR4 function and HIV entry. *Biochem. Pharmacol.* **158**, 402–412 (2018).
41. M. A. Digman, R. Dalal, A. F. Horwitz, E. Gratton, Mapping the number of molecules and brightness in the laser scanning microscope. *Biophys. J.* **94**, 2320–2332 (2008).
42. J. R. Unruh, E. Gratton, Analysis of molecular concentration and brightness from fluorescence fluctuation data with an electron multiplied CCD camera. *Biophys. J.* **95**, 5385–5398 (2008).
43. J. van Unen *et al*., A new generation of FRET sensors for robust measurement of Gαi1, Gαi2 and Gαi3 activation kinetics in single cells. *PLoS One* **11**, e0146789 (2016).
44. W. B. Zhang *et al*., A point mutation that confers constitutive activity to CXCR4 reveals that T140 is an inverse agonist and that AMD3100 and ALX40-4C are weak partial agonists. *J. Biol. Chem.* **277**, 24515–24521 (2002).
45. M. Arimont *et al*., Structural analysis of chemokine receptor-ligand interactions. *J. Med. Chem.* **60**, 4735–4779 (2017).
46. S. B. Peng *et al*., Identification of LY2510924, a novel cyclic peptide CXCR4 antagonist that exhibits antitumor activities in solid tumor and breast cancer metastatic models. *Mol. Cancer Ther.* **14**, 480–490 (2015).
47. S. Thiele, J. Mungalpara, A. Steen, M. M. Rosenkilde, J. Våbenø, Determination of the binding mode for the cyclopentapeptide CXCR4 antagonist FC131 using a dual approach of ligand modifications and receptor mutagenesis. *Br. J. Pharmacol.* **171**, 5313–5329 (2014).
48. M. P. Wescott *et al*., Signal transmission through the CXC chemokine receptor 4 (CXCR4) transmembrane helices. *Proc. Natl. Acad. Sci. U.S.A.* **113**, 9928–9933 (2016).
49. B. Lee, M. Sharron, L. J. Montaner, D. Weissman, R. W. Doms, Quantification of CD4, CCR5, and CXCR4 levels on lymphocyte subsets, dendritic cells, and differentially conditioned monocyte-derived macrophages. *Proc. Natl. Acad. Sci. U.S.A.* **96**, 5215–5220 (1999).
50. A. Tabor *et al*., Visualization and ligand-induced modulation of dopamine receptor dimerization at the single molecule level. *Sci. Rep.* **6**, 33233 (2016).
51. P. M. Dijkman *et al*., Dynamic tuneable G protein-coupled receptor monomer-dimer populations. *Nat. Commun.* **9**, 1710 (2018).
52. J. Heuninck *et al*., Context-dependent signaling of CXC chemokine receptor 4 and atypical chemokine receptor 3. *Mol. Pharmacol.* **96**, 778–793 (2019).
53. C. Perpiñá-Viciano *et al*., Kinetic analysis of the early signaling steps of the human chemokine receptor CXCR4. *Mol. Pharmacol.* **98**, 72–87 (2020).
54. C. E. Mona *et al*., Design, synthesis, and biological evaluation of CXCR4 ligands. *Org. Biomol. Chem.* **14**, 10298–10311 (2016).
55. R. Lamichhane *et al*., Single-molecule view of basal activity and activation mechanisms of the G protein-coupled receptor β2AR. *Proc. Natl. Acad. Sci. U.S.A.* **112**, 14254–14259 (2015).
56. G. G. Gregorio *et al*., Single-molecule analysis of ligand efficacy in β_2AR-G-protein activation. *Nature* **547**, 68–73 (2017).
57. D. Hilger *et al*., Structural insights into differences in G protein activation by family A and family B GPCRs. *Science* **369**, eaba3373 (2020).
58. N. Smith *et al*., Control of TLR7-mediated type i IFN signaling in pDCs through CXCR4 engagement-A new target for lupus treatment. *Sci. Adv.* **5**, eaav9019 (2019).
59. O. Zirafi *et al*., Discovery and characterization of an endogenous CXCR4 antagonist. *Cell Rep.* **11**, 737–747 (2015).
60. K. Jaqaman *et al*., Robust single-particle tracking in live-cell time-lapse sequences. *Nat. Methods* **5**, 695–702 (2008).
61. R. Serfling *et al*., Quantitative single-residue bioorthogonal labeling of G protein-coupled receptors in live cells. *ACS Chem. Biol.* **14**, 1141–1149 (2019).
62. A. Trullo, V. Corti, E. Arza, V. R. Caiolfa, M. Zamai, Application limits and data correction in number of molecules and brightness analysis. *Microsc. Res. Tech.* **76**, 1135–1146 (2013).
63. C. Dominguez, R. Boelens, A. M. J. J. Bonvin, HADDOCK: A protein-protein docking approach based on biochemical or biophysical information. *J. Am. Chem. Soc.* **125**, 1731–1737 (2003).
64. Y. Yoshikawa, K. Kobayashi, S. Oishi, N. Fujii, T. Furuya, Molecular modeling study of cyclic pentapeptide CXCR4 antagonists: New insight into CXCR4-FC131 interactions. *Bioorg. Med. Chem. Lett.* **22**, 2146–2150 (2012).
65. L. O. Gerlach *et al*., Metal ion enhanced binding of AMD3100 to Asp262 in the CXCR4 receptor. *Biochemistry* **42**, 710–717 (2003).
66. M. M. Rosenkilde *et al*., Molecular mechanism of action of monocyclam versus bicyclam non-peptide antagonists in the CXCR4 chemokine receptor. *J. Biol. Chem.* **282**, 27354–27365 (2007).
67. M. M. Rosenkilde *et al*., Molecular mechanism of AMD3100 antagonism in the CXCR4 receptor: Transfer of binding site to the CXCR3 receptor. *J. Biol. Chem.* **279**, 3033–3041 (2004).
68. T. Ngo *et al*., Crosslinking-guided geometry of a complete CXC receptor-chemokine complex and the basis of chemokine subfamily selectivity. *PLoS Biol.* **18**, e3000656 (2020).